International Journal of Engineering Science 227 (2026) 104598

Contents lists available at ScienceDirect

International Journal of Engineering Science

journal homepage: www.elsevier.com/locate/ijengsci

Full length article

Large-strains beam formulation from hyperelasticity

Stefano Sirotti [a,*], Matteo Pelliciari [a], Angelo Marcello Tarantino [a]

[a] Department of Engineering "Enzo Ferrari", University of Modena and Reggio Emilia, via P. Vivarelli 10, 41125 Modena, Italy

ARTICLE INFO

Keywords:
Large deformations
Reissner model
Volumetric behavior
Shear deformations
Three-point bending
Polymer nanocomposites

ABSTRACT

We present a formulation for large-strains analyses of beams made of hyperelastic materials. Building upon Reissner beam theory, we establish a connection between beam internal forces and the stress components of continuum hyperelasticity. The transition from the three-dimensional continuum to the one-dimensional beam approximation is achieved by constraining the volumetric part of the strain energy function. As a result, closed-form expressions for the beam internal forces as functions of the material stress–strain response are obtained. The formulation is then specialized to carbon nanotubes-based polymer nanocomposites (CNT-based PNCs) and validated against data from three-point bending tests on PNC beams. To the best of our knowledge, this is the first continuum mechanics-based beam formulation directly validated against experimental material responses. Further validation is provided through two-dimensional finite element (FE) simulations under plane stress conditions. The proposed formulation captures the nonlinear constitutive behavior of continuum models while retaining the simplicity of a one-dimensional beam description. It provides a foundation for more complex analyses of hyperelastic slender structures undergoing large strains.

1. Introduction

The analysis of beams undergoing large deformations has a long tradition, dating back to the classical treatment of the elastica by Euler (1744). Subsequently, several authors introduced axial extensibility and shear deformability to investigate their influence on the critical load of structural elements. In the geometrically nonlinear regime, shear deformability allows for multiple definitions of the beam internal forces. Within this context, two main interpretations of shear deformation were developed. The first approach, proposed by Engesser (1891), is less popular (Firouzi et al., 2024; Lenci & Rega, 2016) and assumes the normal force and the shear force directed along the tangent to the beam axis and normal to the beam axis, respectively (Ziegler, 1982). The second approach, originally proposed by Haringx (1942), considers the normal force to be directed along the normal to the cross-section and the shear force to lie in the tangential direction. Reissner (1972) generalized this formulation developing a theory of geometrically-exact and axially extensible beams. The Reissner model obtained a great success for the analysis of beams under large deformations and became widely adopted (Batista, 2016; Humer, 2013; Simo et al., 1984). More recently, Paradiso et al. (2025) proposed a shearable beam based on an origami-like microstructure, which reduces to the Engesser and Haringx beams for particular values of the internal length parameter.

The aforementioned works assumed linear relationships between internal forces and strain measures. Therefore, although large deformations were considered, the material was supposed to remain within the linear elastic regime. For many materials, however, this assumption is not realistic, and material nonlinearities must be considered to obtain a consistent structural response. In his pioneering work, Reissner (1972) postulated the existence of potentially nonlinear relations between the beam internal forces

* Corresponding author.
E-mail addresses: stefano.sirotti@unimore.it (S. Sirotti), matteo.pelliciari@unimore.it (M. Pelliciari), angelomarcello.tarantino@unimore.it (A.M. Tarantino).

https://doi.org/10.1016/j.ijengsci.2026.104598
Received 27 April 2026; Received in revised form 27 May 2026; Accepted 3 June 2026

Available online 14 June 2026

and the strain measures, claiming that such relations should, in principle, be determined experimentally. Subsequently, many authors tried to establish a solid connection between beam internal forces and stress components in the framework of continuum mechanics. Magnusson et al. (2001) derived the classical linear relations for the normal force and the bending moment of an Euler–Bernoulli beam starting from a linear relation between the Biot stress and the Biot strain at the material level. Other authors, such as Humer and Irschik (2011) and Irschik and Gerstmayr (2009), showed that other linear stress–strain relations at the material level may lead to nonlinear relations for the beam internal forces, as is the case for the St. Venant-Kirchhoff model. Irschik and Gerstmayr (2009) further established a continuum mechanics-based framework for the kinematics of Reissner beam theory. Their formulation was first developed for Euler–Bernoulli beams and later extended to shear-deformable beams in Irschik and Gerstmayr (2011).

Other authors have attempted to incorporate nonlinear hyperelastic models into beam formulations. Attard (2003) derived expressions for the normal and shear stresses in a beam by linearizing a compressible Neo-Hookean hyperelastic law. Maqueda and Shabana (2007) developed a finite element framework for beams with hyperelastic material laws. Lubbers et al. (2017) adopted a Neo-Hookean model to study the buckling of elastomeric columns, employing a second-order expansion of the stress. Humer and Irschik (2009) performed a series expansion of the hyperelastic model proposed by Palmov (1998) to study the deformation of a beam with unknown length.

Despite these contributions, some critical aspects of the connection between continuum hyperelasticity and beam theories remain unclear. In particular, beam formulations typically assume transversely rigid cross-sections, thereby constraining the volumetric behavior of the material. In contrast, three-dimensional continuum mechanics models adopt the real volumetric behavior of the material, which in general differs from that required by the beam model. Attard (2003), Attard and Hunt (2008) and Attard and Kim (2010) pointed out this inconsistency, but, to address this issue, they allowed for reactive forces on the lateral surfaces of the beam, thereby accepting to satisfy equilibrium only approximately. Moreover, so far, none of the continuum mechanics-based models proposed has been applied to experimental data. Therefore, a validation of these formulations against real material responses still lacks.

In light of these considerations, we establish a comprehensive connection between the large-displacements, large-strains beam theory and three-dimensional hyperelasticity. We assume the kinematics of deformation for planar beams proposed by Reissner in his geometrically-exact beam model. We then derive closed-form expressions for the beam internal forces as functions of the nonlinear stress–strain response of hyperelastic materials. In passing from the three-dimensional continuum to the one-dimensional beam approximation, care must be taken to satisfy the assumption of transversely rigid cross-sections. We address this issue by appropriately reformulating the volumetric contribution to the strain energy function.

Subsequently, we specialize the formulation to polymeric beams reinforced with carbon nanotubes (CNTs) adopting the hyperelastic model that we proposed in Pelliciari et al. (2025b). The interest in CNT-based polymer nanocomposites (PNCs) is due to the exceptional mechanical and functional performance of these materials even at relatively low filler loadings (Fu et al., 2019; Kim et al., 2010; Matos et al., 2018; Moniruzzaman & Winey, 2006). However, so far their study has been limited to simple homogeneous deformation states, primarily simple tension (Cantournet et al., 2007; Islam et al., 2023). The analysis of these materials under more complex deformation states is thus worth of investigation, in order to exploit their properties for a wide range of technological applications (Miculescu et al., 2016; Qin et al., 2015; Wang & Zhu, 2011). Here, we apply the proposed beam formulation to experimental data obtained from three-point bending tests performed on CNT-based PNC beams. PNC beams with different CNT contents are tested under the clamped-clamped and hinged-hinged configurations. In addition, finite element (FE) simulations of two-dimensional beams under plane stress conditions are carried out to validate the proposed model. It should be emphasized that the proposed beam formulation is developed within the framework of local elasticity theory. Although the constitutive model is specialized to polymer composites reinforced with nanoparticles, the structural scale considered in the present work remains macroscopic. Consequently, nonlocal effects are not expected to play a significant role and are therefore neglected.

The paper is structured as follows. Section 2 describes the kinematics of the beam model. The equilibrium equations are written and the connection between the beam internal forces and the stress components of continuum mechanics is established by the Principle of Virtual Works. Section 3 defines the framework for computing closed-form expressions for the beam stress resultants from the strain energy function of a hyperelastic materials. These expressions are then specialized to CNT-based PNCs, adopting the hyperelastic model that we developed in Pelliciari et al. (2025b). In Section 4 we present the three-point bending tests carried out on PNC beams, along with the numerical solution of the boundary value problems, the FE simulations and the discussion of the results. Finally, conclusions are drawn in Section 5.

2. The beam model

In this section, we present the large-displacement, large-strains beam model adopted in this work. We first describe the beam kinematics, following the continuum mechanics-based interpretation developed by Irschik and Gerstmayr (2011) for shearable beams based on the Reissner (1972) model. We then derive the equilibrium equations of a differential beam element and establish the connection between the beam internal forces and the stress components of continuum mechanics through the Principle of Virtual Work.

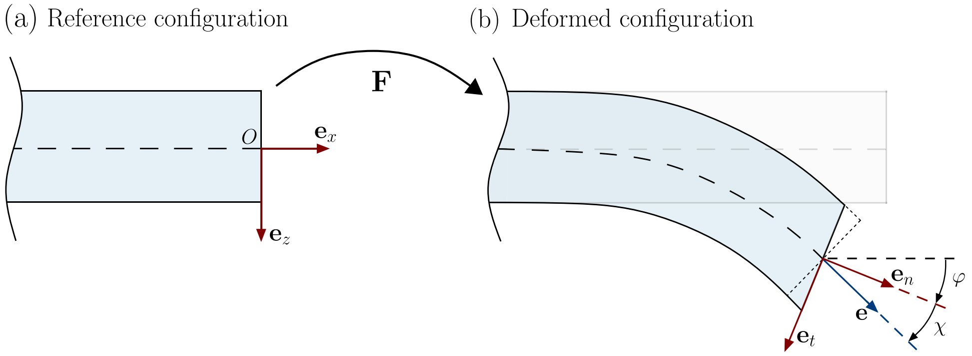

Fig. 1. Kinematics of deformation of a planar beam. The beam is assumed to be axially extensible and shear-deformable. After deformation, the cross-section rotates by an angle $\varphi(x)$. Due to shear deformation, the tangent vector $\mathbf{e}$ to the beam axis forms an angle $\chi(x)$ with the normal vector $\mathbf{e}_n$ to the cross-section. The beam cross-section is assumed to be rigid, meaning that no transverse deformation occurs along the $\mathbf{e}_y$ and $\mathbf{e}_z$ directions.

2.1. Kinematics

We consider a planar beam with a straight axis in the undeformed configuration, as shown in Fig. 1(a). The beam is assumed axially extensible and shear-deformable. For the description of the deformation, we assume a Cartesian reference frame $\{x, y, z\}$ defined by the unit vectors $\mathbf{e}_x$, $\mathbf{e}_y$, $\mathbf{e}_z$. Vector $\mathbf{e}_x$ is directed along the beam axis, whereas $\mathbf{e}_y$ and $\mathbf{e}_z$ span the beam cross-section. After deformation, a generic cross-section rotates by an angle $\varphi(x)$ with respect to the x-axis remaining plane and undistorted. However, due to shear deformation, its unit normal vector forms an angle $\chi(x)$ with the tangent to the beam axis, corresponding to the classical Timoshenko assumption. The unit vectors normal and tangential to the cross-section in the deformed configuration read respectively (see Fig. 1(b))

$$\mathbf{e}_n = \cos\varphi\,\mathbf{e}_x + \sin\varphi\,\mathbf{e}_z, \tag{1}$$

$$\mathbf{e}_t = -\sin\varphi\,\mathbf{e}_x + \cos\varphi\,\mathbf{e}_z. \tag{2}$$

The position vector of a generic point P in the undeformed configuration is $\mathbf{x} = x\mathbf{e}_x + y\mathbf{e}_y + z\mathbf{e}_z$. Its position in the deformed configuration reads

$$\mathbf{r}(x, y, z) = \mathbf{r}_0(x) + y\mathbf{e}_y + z\mathbf{e}_t(x), \tag{3}$$

where $\mathbf{r}_0$ is the deformation vector of the beam axis. The deformation gradient is defined as

$$\mathbf{F} = \frac{\partial \mathbf{r}}{\partial \mathbf{x}} = (\mathbf{r}_0' + z\mathbf{e}_t') \otimes \mathbf{e}_x + \mathbf{e}_y \otimes \mathbf{e}_y + \mathbf{e}_t \otimes \mathbf{e}_z, \tag{4}$$

where the prime denotes differentiation with respect to x. Since $\mathbf{r}_0'$ is tangent to the beam axis, in general it will not be normal to the beam cross-section due to the shear angle χ. Denoting the direction tangent to the beam axis with the unit vector $\mathbf{e}$, the vector $\mathbf{r}_0'$ can be expressed as

$$\mathbf{r}_0' = \Lambda\mathbf{e}, \quad \text{with} \quad \Lambda = \|\mathbf{r}_0'\|, \quad \mathbf{e} = \cos(\varphi+\chi)\mathbf{e}_x + \sin(\varphi+\chi)\mathbf{e}_z, \tag{5}$$

where Λ represents the *stretch* of an element of the beam axis. The vector $\mathbf{r}_0'$ can then be projected along the Cartesian reference frame as

$$\mathbf{r}_0' \cdot \mathbf{e}_x = r_{0_x}' = \Lambda\cos(\varphi+\chi), \tag{6}$$

$$\mathbf{r}_0' \cdot \mathbf{e}_z = r_{0_z}' = \Lambda\sin(\varphi+\chi). \tag{7}$$

Using Eqs. (2), (6), (7), and computing $\mathbf{e}_t'$ from (2), the deformation gradient $\mathbf{F}$ assumes the following representation in the Cartesian frame:

$$\mathbf{F} = \begin{bmatrix} \Lambda\cos(\chi+\varphi) - z\varphi'\cos\varphi & 0 & -\sin\varphi \\ 0 & 1 & 0 \\ \Lambda\sin(\chi+\varphi) - z\varphi'\sin\varphi & 0 & \cos\varphi \end{bmatrix}. \tag{8}$$

The determinant of $\mathbf{F}$ measures the local variation of volume and reads

$$J = \det\mathbf{F} = \Lambda\cos\chi - z\varphi'. \tag{9}$$

The right Cauchy–Green tensor $\mathbf{C} = \mathbf{F}^{\mathrm{T}}\mathbf{F}$ reads

$$\mathbf{C} = \begin{bmatrix} \Lambda^2 - 2\Lambda z\varphi' \cos\chi + (z\varphi')^2 & 0 & \Lambda \sin\chi \\ 0 & 1 & 0 \\ \Lambda \sin\chi & 0 & 1 \end{bmatrix}, \tag{10}$$

and the Green–Lagrange strain tensor can be computed as $\mathbf{E} = (\mathbf{C} - \mathbf{I})/2$. We now introduce the generalized strain measures

$$\kappa = \varphi', \quad \lambda = \Lambda \cos\chi, \quad \gamma = \Lambda \sin\chi, \tag{11}$$

corresponding to the *bending strain*, the *axial force stretch*, and the *shear strain*, as defined by Reissner (1972) in his pioneering work.[1] The strain tensors $\mathbf{C}$ and $\mathbf{E}$, and the Jacobian J, are expressed as functions of the generalized strains as

$$\mathbf{C} = \begin{bmatrix} (\lambda - z\kappa)^2 + \gamma^2 & 0 & \gamma \\ 0 & 1 & 0 \\ \gamma & 0 & 1 \end{bmatrix}, \quad \mathbf{E} = \frac{1}{2}\begin{bmatrix} (\lambda - z\kappa)^2 + \gamma^2 - 1 & 0 & \gamma \\ 0 & 0 & 0 \\ \gamma & 0 & 0 \end{bmatrix}, \quad J = \lambda - z\kappa. \tag{12}$$

As pointed out by Irschik and Gerstmayr (2011), expressing $\mathbf{C}$, $\mathbf{E}$, and J as functions of the generalized strains κ, λ, and γ demonstrates that these quantities are consistent strain measures also from the viewpoint of continuum mechanics, since the strain tensors are material frame-indifferent.

From tensors $\mathbf{C}$ and $\mathbf{E}$ we observe that there is no deformation along the transverse directions y and z, hence the beam kinematics assumes rigid cross-sections. This assumption reflects the beam approximation that deformation along the longitudinal axis dominates over that in the cross-section. From a constitutive standpoint, however, this assumption constrains the material volumetric response, as a local volume change equal to $J = \lambda - zk$ must necessarily occur. This implies a Poisson's ratio $\nu = 0$, independent of the applied deformation. However, since most materials have a Poisson's ratio in the range $\nu \in (0, 0.5)$, a discrepancy between the material properties and the beam kinematic assumption arises. This issue will be carefully addressed in Sections 3.1 and 3.2. We remark that some authors have proposed three-dimensional beam models that provide a complete description of cross-sectional deformation, see, e.g., Falope et al. (2019).

2.2. Equilibrium and virtual works

We assume a set of distributed loads $p(x)$, $q(x)$, and $m(x)$ acting on an infinitesimal beam element dx in the undeformed configuration, as shown in Fig. 2(a). In the deformed configuration, the external loads are balanced by the internal forces N, T, and M, defined respectively as the normal force, the shear force, and the bending moment. Since in shear-deformable beams the direction tangent to the beam axis does not coincide with the normal to the cross-section, the definition of the normal force and the shear force is not unique. Here, we follow the popular approach of Reissner (1972), where the normal force is directed along the normal direction to the cross-section and the shear force is tangent to the cross-section. With reference to Fig. 2(b), the equilibrium equations read

$$(N \cos\varphi - T \sin\varphi)' + p = 0, \tag{13}$$

$$(N \sin\varphi + T \cos\varphi)' + q = 0, \tag{14}$$

$$M' + \Lambda(T \cos\chi - N \sin\chi) + m = 0. \tag{15}$$

To complete the formulation of the problem, constitutive relations need to be established between the internal forces N, T, M and the generalized strains λ, γ, κ.

In deriving his beam theory, Reissner postulated the existence of (generally nonlinear) relations between the internal forces and the generalized strains, leaving their determination to experiments. Subsequently, many authors sought to establish a consistent connection between the beam internal forces and the stress–strain relations of continuum mechanics. Irschik and Gerstmayr (2009) provided the most comprehensive continuum mechanics interpretation of Reissner theory for Euler–Bernoulli beams, later extending the framework to shear-deformable beams (Irschik & Gerstmayr, 2011). Following their approach, we assume the existence of the symmetric second Piola–Kirchhoff stress tensor $\mathbf{S}$, whose representation in the Cartesian reference frame is

$$\mathbf{S} = \begin{bmatrix} S_{xx} & S_{xy} & S_{xz} \\ S_{xy} & S_{yy} & S_{yz} \\ S_{xz} & S_{yz} & S_{zz} \end{bmatrix}. \tag{16}$$

The virtual work of the internal forces per unit length, within the framework of continuum mechanics, can be expressed as[2]

$$\delta W_{\mathrm{int}} = \int_A \mathbf{S} : \delta\mathbf{E}\, dA. \tag{17}$$

[1] Reissner originally postulated the existence of the generalized strain measures, successively deriving their expression by means of the Principle of Virtual Works. Instead of λ, he defined the *axial force strain as* $\epsilon = \Lambda \cos\chi - 1$.

[2] Any other pair of energetically conjugate stress–strain tensors can be used, see e.g. Humer and Irschik (2011).

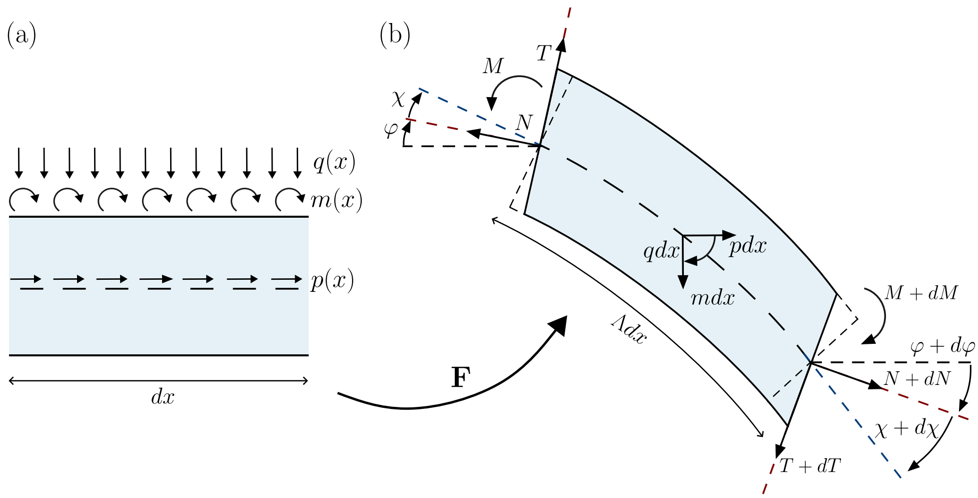

Fig. 2. Equilibrium of an infinitesimal beam element dx. (a) Distributed loads acting in the reference configuration and (b) equilibrium of the internal forces in the deformed configuration.

Equating this expression to the virtual work per unit beam length of the internal forces, $\delta W_{\text{int}} = N\delta\lambda + T\delta\gamma + M\delta\kappa$, recalling the expression of $\mathbf{E}$ in (12), and computing the variation of the generalized strain measures

$$\delta\kappa = \delta\varphi', \quad \delta\lambda = \delta\Lambda\cos\chi - \delta\chi\Lambda\sin\chi, \quad \delta\gamma = \delta\Lambda\sin\chi + \delta\chi\Lambda\cos\chi, \tag{18}$$

we obtain the expression of the internal forces in terms of the stress components[3]:

$$N = \int_A S_{xx}\left(\Lambda\cos\chi - z\varphi'\right) dA = \int_A S_{xx} J\, dA, \tag{19}$$

$$T = \int_A \left(S_{xx}\Lambda\sin\chi + S_{xz}\right) dA = \int_A \left(S_{xx}\gamma + S_{xz}\right)\, dA, \tag{20}$$

$$M = -\int_A S_{xx}\left(\Lambda\cos\chi - z\varphi'\right) z\, dA = -\int_A S_{xx} J z\, dA. \tag{21}$$

It is interesting to observe that a coupling between the shear force and the normal stress arises naturally as a consequence of the adopted continuum mechanics framework. This is not the case in the Reissner beam model.[4] A continuum mechanics-based justification of Eqs. (19)–(21) is provided by Irschik and Gerstmayr (2011).

Eqs. (19)–(21) allow the computation of the beam internal forces once the stress tensor components S_{xx}, S_{xz}, and S_{zz} are known, thereby providing a direct connection between the stress resultants of the beam theory and the stress–strain response at the material level in continuum mechanics.

3. Internal forces from hyperelasticity

In this section, we derive the expressions of the stress components of a hyperelastic material defined by a strain energy function W. We then establish closed-form expressions for the beam internal forces N, T, and M as functions of the stress components of continuum mechanics. Finally, we specialize these relations to CNT-based polymer nanocomposites.

3.1. The strain energy function and the stress tensor

The mechanical response of an isotropic hyperelastic material is determined by a strain energy function $W = W(I_1, I_2, I_3)$, where I_1, I_2, and I_3 are the principal invariants of the Cauchy–Green strain tensor $\mathbf{C}$, defined as

$$I_1 = \operatorname{tr}\mathbf{C}, \quad I_2 = \frac{1}{2}\left[(\operatorname{tr}\mathbf{C})^2 - \operatorname{tr}\left(\mathbf{C}^2\right)\right], \quad I_3 = \det\mathbf{C}. \tag{22}$$

[3] In Eq. (21), a minus sign has been added to the integral in order to ensure consistency with the sign conventions adopted for the bending strain and the bending moment. In particular, a positive bending strain corresponds to a positive bending moment (see Figs. 1 and 2).

[4] However, in his application to the buckling of circular rings, Reissner (1972) allows a coupling between T and N by defining the shear strain as $\gamma = BT/(1+\lambda BN)$, where B is a proportionality constant and $\lambda \in [0,1]$ is a coupling parameter.

For compressible materials, it is convenient to separate volumetric and deviatoric contributions by decomposing the strain energy function as (Sansour, 2008):

$$W = W_d\left(\bar{I}_1, \bar{I}_2\right) + W_h(J), \tag{23}$$

where $\bar{I}_1 = I_1/J^{2/3}$ and $\bar{I}_2 = I_2/J^{4/3}$ are the isochoric invariants, and $J = \sqrt{I_3}$. For incompressible materials, every deformation is isochoric, $J = 1$, and the energy reduces to $W_{inc} = W_d(I_1, I_2)$. This it typically the case for polymers, most of which exhibit negligible volume changes even under large deformations (Boyce & Arruda, 2000; Treloar, 1975). However, as discussed in Section 2.1, the beam kinematics assumes transversely rigid cross-sections. To satisfy this kinematic constraint, local volume changes must be permitted, corresponding to $J = \lambda - z\kappa$. Consequently, regardless of whether the actual material is compressible or incompressible, in the beam model its volumetric response is dictated by the kinematical constraint of transversely rigid cross-sections. For this reason, in the following we assume a strain energy function of the form in Eq. (23), with the volumetric part defined as (Simo, 1988):

$$W_h(J) = \frac{K}{2}(J-1)^2. \tag{24}$$

The parameter K should not be interpreted as the physical bulk modulus of the material. Instead, it acts as a penalty parameter enforcing the volumetric deformation required by the beam kinematics.[5]

The second Piola–Kirchhoff stress tensor is computed as

$$\mathbf{S} = 2\frac{\partial W}{\partial \mathbf{C}} = 2\left(\frac{\partial W_d}{\partial \bar{I}_1}\frac{\partial \bar{I}_1}{\partial \mathbf{C}} + \frac{\partial W_d}{\partial \bar{I}_2}\frac{\partial \bar{I}_2}{\partial \mathbf{C}} + \frac{\partial W_h}{\partial J}\frac{\partial J}{\partial \mathbf{C}}\right), \tag{25}$$

with the tensor $\mathbf{C}$ given in (12) and

$$\frac{\partial \bar{I}_1}{\partial \mathbf{C}} = J^{-2/3}\left(\mathbf{I} - \frac{1}{3}I_1\mathbf{C}^{-1}\right), \quad \frac{\partial \bar{I}_2}{\partial \mathbf{C}} = J^{-4/3}\left(I_1\mathbf{I} - \mathbf{C} - \frac{2}{3}I_2\mathbf{C}^{-1}\right), \quad \frac{\partial J}{\partial \mathbf{C}} = \frac{1}{2}J\mathbf{C}^{-1}. \tag{26}$$

The expression of K is determined by imposing the zero-traction condition along the y-direction normal to the beam plane, namely $S_{yy} = 0$, which yields

$$K = \frac{2\left[J^{2/3}\left(J^2+\gamma^2-1\right)\overline{w}_1 + \left(J^2-\gamma^2-1\right)\overline{w}_2\right]}{3(J-1)J^{7/3}}, \tag{27}$$

where $\overline{w}_1 = \partial W_d/\partial \bar{I}_1$, $\overline{w}_2 = \partial W_d/\partial \bar{I}_2$. Since $\bar{I}_1$ and $\bar{I}_2$ can be written as functions of the generalized strains,

$$\bar{I}_1 = \frac{2+J^2+\gamma^2}{J^{2/3}}, \quad \bar{I}_2 = \frac{1+2J^2+\gamma^2}{J^{4/3}}, \tag{28}$$

in the following J and γ^2 are adopted as independent variables. Evaluating Eq. (27) in the reference configuration, we obtain the linear bulk modulus:

$$K_0 = \frac{4}{3}\left(\overline{w}_1^0 + \overline{w}_2^0\right), \tag{29}$$

where

$$\overline{w}_1^0 = \left.\frac{\partial W_d}{\partial \bar{I}_1}\right|_{\mathbf{C}=\mathbf{I}}, \qquad \overline{w}_2^0 = \left.\frac{\partial W_d}{\partial \bar{I}_2}\right|_{\mathbf{C}=\mathbf{I}}. \tag{30}$$

Recalling the expression of the linear shear modulus, $G = 2(\overline{w}_1^0 + \overline{w}_2^0)$, it follows directly that the Poisson's ratio vanishes:

$$\nu = \frac{3K_0 - 2G}{2\left(3K_0 + G\right)} = 0, \tag{31}$$

which is consistent with the assumption of transversely rigid cross-sections. Substituting Eq. (27) into Eq. (25), the second Piola–Kirchhoff stress tensor $\mathbf{S}$ becomes:

$$\mathbf{S} = \frac{2}{J^{10/3}}\begin{bmatrix} J^{2/3}\left(J^2-1\right)\overline{w}_1 + \left(J^2-\gamma^2-1\right)\overline{w}_2 & 0 & \gamma\left[J^{2/3}\overline{w}_1 + \left(\gamma^2+1\right)\overline{w}_2\right] \\ 0 & 0 & 0 \\ \gamma\left[J^{2/3}\overline{w}_1 + \left(\gamma^2+1\right)\overline{w}_2\right] & 0 & -\gamma^2\left[J^{2/3}\overline{w}_1 + \left(J^2+\gamma^2+1\right)\overline{w}_2\right] \end{bmatrix}. \tag{32}$$

Due to shear deformation, a normal stress S_{zz} in the z-direction arises. Within the framework of continuum mechanics, a non-vanishing traction at the boundary is required to ensure equilibrium, as in the case of a body subjected to a finite simple shear deformation (Rivlin, 1948; Sadd, 2018). However, due to the rigid cross-sections assumption, in the beam model this normal stress does not contribute to the virtual work, as shown by Eqs. (19)–(21). This is consistent with classical beam theories, which assume negligible normal stresses in the transverse directions. From Eq. (32), we note that the S_{zz} component depends on γ^2. Since, for slender beams, the amount of shear γ is typically small compared to unity, the quadratic dependence on γ^2 makes the S_{zz} component negligible compared to the others in most applications even within the continuum framework.

[5] To enforce the kinematical constraint of transversely rigid cross-sections, Attard (2003) allowed for reactive stresses on the lateral sides of the cross-section, satisfying equilibrium only approximately.

3.2. Stress resultants for the beam model

Recalling Eqs. (19)–(21), we define the normal stress σ_x and the tangential stress τ_{xz} as

$$\begin{aligned}\sigma_x &= S_{xx}J,\\ \tau_{xz} &= S_{xx}\gamma + S_{xz},\end{aligned} \tag{33}$$

and are functions of the generalized strain measures λ, γ, and κ. The beam internal forces N, T, and M are obtained by integration over the cross-sectional area A:

$$N = \int_A \sigma_x dA, \quad T = \int_A \tau_{xz} dA, \quad M = -\int_A \sigma_x z dA. \tag{34}$$

For generic nonlinear hyperelastic materials, these integrals cannot be evaluated in a closed form, even for the simplest case of a rectangular cross-section. To obtain analytical expressions, we approximate the stress components using a third-order expansion in κ. The power-series expansion of σ_x and τ_{xz} around $\kappa = 0$ yields

$$\begin{aligned}\sigma_x^* &= \sum_{n=0}^{3} \frac{1}{n!}\frac{\partial^n \sigma_x}{\partial \kappa^n}\Big|_{\kappa=0} \kappa^n + \mathcal{O}\left(\kappa^4\right),\\ \tau_{xz}^* &= \sum_{n=0}^{3} \frac{1}{n!}\frac{\partial^n \tau_{xz}}{\partial \kappa^n}\Big|_{\kappa=0} \kappa^n + \mathcal{O}\left(\kappa^4\right),\end{aligned} \tag{35}$$

where the derivatives of the stress components with respect to κ are reported in Appendix A.

Integrating σ_x^* and τ_{xz}^* according to Eq. (34), we obtain

$$N = \mathcal{F}_N\left(\lambda, \gamma^2\right) A + \mathcal{G}_N\left(\lambda, \gamma^2\right) I_y \kappa^2, \tag{36}$$

$$T = \gamma \mathcal{F}_T\left(\lambda, \gamma^2\right) A_t + \gamma \mathcal{G}_T\left(\lambda, \gamma^2\right) I_y \kappa^2, \tag{37}$$

$$M = \mathcal{F}_M\left(\lambda, \gamma^2\right) I_y \kappa + \mathcal{G}_M\left(\lambda, \gamma^2\right) K_y \kappa^3, \tag{38}$$

where

$$A = \int_A dA, \quad I_y = \int_A z^2 dA, \quad K_y = \int_A z^4 dA, \quad A_t = k_t A, \tag{39}$$

represent respectively the cross-sectional area, the second moment of area, the fourth-order moment of area, and the shear area, with k_t denoting the shear correction factor. The normal force and the shear force are even functions of κ, whereas the bending moment is an odd function, as expected from symmetry considerations. The expansion up to third order in κ ensures the inclusion of the dominant nonlinear effects while preserving compact expressions for the internal forces. The quantities $\mathcal{F}_i$, $\mathcal{G}_i$, with $i = N, T, M$, are nonlinear functions of λ and γ^2 with dimension of stress that depend only on the constitutive law of the material. They are related to the hyperelastic stress components as

$$\begin{aligned}\mathcal{F}_N\left(\lambda, \gamma^2\right) &= \sigma_x\Big|_{\kappa=0}, \quad \mathcal{G}_N\left(\lambda, \gamma^2\right) = \frac{1}{2z^2}\frac{\partial^2 \sigma_x}{\partial \kappa^2}\Big|_{\kappa=0},\\ \mathcal{F}_T\left(\lambda, \gamma^2\right) &= \frac{\tau_{xz}}{\gamma}\Big|_{\kappa=0}, \quad \mathcal{G}_T\left(\lambda, \gamma^2\right) = \frac{1}{2\gamma z^2}\frac{\partial^2 \tau_{xz}}{\partial \kappa^2}\Big|_{\kappa=0},\\ \mathcal{F}_M\left(\lambda, \gamma^2\right) &= -\frac{1}{z}\frac{\partial \sigma_x}{\partial \kappa}\Big|_{\kappa=0}, \quad \mathcal{G}_M\left(\lambda, \gamma^2\right) = -\frac{1}{6z^3}\frac{\partial^3 \sigma_x}{\partial \kappa^3}\Big|_{\kappa=0}.\end{aligned} \tag{40}$$

As discussed in the previous sections, a fictitious volumetric contribution was introduced into the energy to enforce the volumetric behavior required by the beam kinematics. Therefore, the beam model is characterized by a set of parameters which do not represent the response of the actual material, but rather that of an equivalent material with the internal constraint of rigid cross-sections. To ensure a realistic response of the beam model for a given material, the parameters must be calibrated against uniaxial data. The calibrated values differ from those obtained considering the actual volumetric material behavior, but they provide the same uniaxial response.

In contrast, being calibrated against uniaxial data to obtain the correct response in simple tension, the set of parameters of the beam model cannot, in general, predict the correct shear response. To address this, we renounce to describe the entire nonlinear shear response of the material and we linearize the internal forces with respect to the shear strain γ. Since the functions $\mathcal{F}_i$ and $\mathcal{G}_i$ depend on the shear strain only through γ^2, their linearization about $\gamma = 0$ yields

$$\mathcal{F}_i(\lambda, \gamma^2) = \mathcal{F}_i(\lambda, 0) + \mathcal{O}(\gamma^2), \quad \mathcal{G}_i(\lambda, \gamma^2) = \mathcal{G}_i(\lambda, 0) + \mathcal{O}(\gamma^2), \quad \text{with} \quad i = N, T, M. \tag{41}$$

Defining the quantities

$$f_i(\lambda) = \mathcal{F}_i(\lambda, 0), \quad g_i(\lambda) = \mathcal{G}_i(\lambda, 0), \quad \text{with} \quad i = N, T, M, \tag{42}$$

the internal forces assume the final form

$$N = f_N(\lambda) A + g_N(\lambda) I_y \kappa^2, \tag{43}$$

$$T = \gamma f_T(\lambda) A_t + \gamma\, g_T(\lambda) I_y \kappa^2, \tag{44}$$
$$M = f_M(\lambda) I_y \kappa + g_M(\lambda) K_y \kappa^3. \tag{45}$$

The normal force and the bending moment are now independent of the shear strain γ, whereas the shear force depends linearly on it. The functions f_i and g_i depend solely on λ and their expressions follow directly from the adopted hyperelastic law at the continuum level. Despite the complicated forms that f_i and g_i may assume, Eqs. (43)–(45) retain a simple structure.

Although the linearization with respect to γ was primarily introduced for practical reasons, it represents a reasonable approximation from a physical standpoint. Shear deformations become significant only for members with low slenderness, whereas for slender beams their contribution to the overall response is negligible. Consequently, the linearized formulation accurately captures the material behavior in the vast majority of cases of interest. Nevertheless, the shear response of the beam is not yet fully consistent with the actual shear behavior of the material, as the linear shear modulus does not coincide with that of the material. In the beam model, where $\nu = 0$, the shear modulus is given by $G_{beam} = E_{beam}/2$. On the other hand, the shear modulus of the actual material is $G_{mat} = E_{mat}/[2(1+\nu_{mat})]$. Since the material parameters are calibrated to enforce $E_{beam} = E_{mat}$, it follows that

$$G_{beam} = (1+\nu_{mat}) G_{mat}. \tag{46}$$

To recover the correct linear shear response, the effective shear area is adjusted by rescaling the shear correction factor as

$$k_t^* = \frac{1}{1+\nu_{mat}} k_t. \tag{47}$$

Therefore, the shear area in Eq. (44) is now given by $A_t = k_t^* A$ and the beam shear stiffness GA_t is consistent with the properties of the actual material.

3.3. Application to CNT-based polymer nanocomposites

In our previous work (Pelliciari et al., 2025b), we proposed the following strain energy function to characterize the nonlinear mechanical response of CNT-based PNCs:

$$W_{\mathrm{PNC}}(I_1) = (1-\phi_f) W_m + (\phi_f - \xi\phi_a) W_n + \xi\phi_a W_a, \tag{48}$$

where

$$\begin{aligned}
W_m &= \frac{a}{b}\left[1 - e^{-b(I_1-3)}\right] - C_{10}(I_m - 3)\ln\left(1 - \frac{I_1-3}{I_m-3}\right),\\
W_n &= \psi_n\left(1 + \frac{\psi_n}{\Psi_n}\right)^{-1}, \quad \text{with} \quad \psi_n = \frac{3}{8}E_n\left[\left(\frac{I_1}{3}\right)^{4/3} - 1\right],\\
W_a &= \psi_a\left(1 + \frac{\psi_a}{\Psi_a}\right)^{-1}, \quad \text{with} \quad \psi_a = \frac{1}{2}E_a\left(\frac{I_1}{3} - 1\right),
\end{aligned} \tag{49}$$

are respectively the contributions to the strain energy function given by the matrix, the nanofillers and the agglomerates. Parameters ξ and ϕ_a represent respectively the volume fraction of agglomerates and the fraction of nanofillers within the agglomerates, and depend on the filler content ϕ_f. The parameters E_n and E_a are the *effective moduli* of nanofillers and agglomerates respectively, whereas Ψ_n and Ψ_a are limiting energies which identify the onset of debonding of nanofillers and agglomerates from the matrix. The complete formulation of the model and the expressions of quantities ξ, ϕ_a, E_n, E_a, Ψ_n, and Ψ_a are recalled in Appendix B.

The proposed energy was originally developed for incompressible materials, as volume changes in polymer nanocomposites are negligible. Here, following the framework described in the previous section, we add a volumetric part to enforce the beam kinematic constraint. According to the decomposition into its deviatoric and volumetric parts, the strain energy function now reads:

$$W = W_{\mathrm{PNC}}(\bar{I}_1) + W_h(J) = W_{\mathrm{PNC}}(\bar{I}_1) + \frac{K}{2}(J-1)^2. \tag{50}$$

The derivatives with respect to the isochoric invariants are

$$\begin{aligned}
\overline{w}_1 &= (1-\phi_f)\left[a e^{-b(\bar{I}_1-3)} + \frac{C_{10}(I_m-3)}{I_m - \bar{I}_1}\right] + \frac{6E_a\xi\Psi_a^2\phi_a}{\left[E_a(\bar{I}_1-3) + 6\Psi_a\right]^2} + \frac{32\, E_n (9\bar{I}_1)^{1/3}\Psi_n^2(\phi_f - \xi\phi_a)}{\left[E_n\left(3^{2/3}\bar{I}_1^{4/3} - 9\right) + 24\Psi_n\right]^2},\\
\overline{w}_2 &= 0,
\end{aligned} \tag{51}$$

and the parameter K is computed from Eq. (27). The second Piola–Kirchhoff stress tensor $\mathbf{S}$, given in Eq. (32), reduces to

$$\mathbf{S} = 2\frac{\overline{w}_1}{J^{8/3}}\begin{bmatrix} J^2-1 & 0 & \gamma \\ 0 & 0 & 0 \\ \gamma & 0 & -\gamma^2 \end{bmatrix}. \tag{52}$$

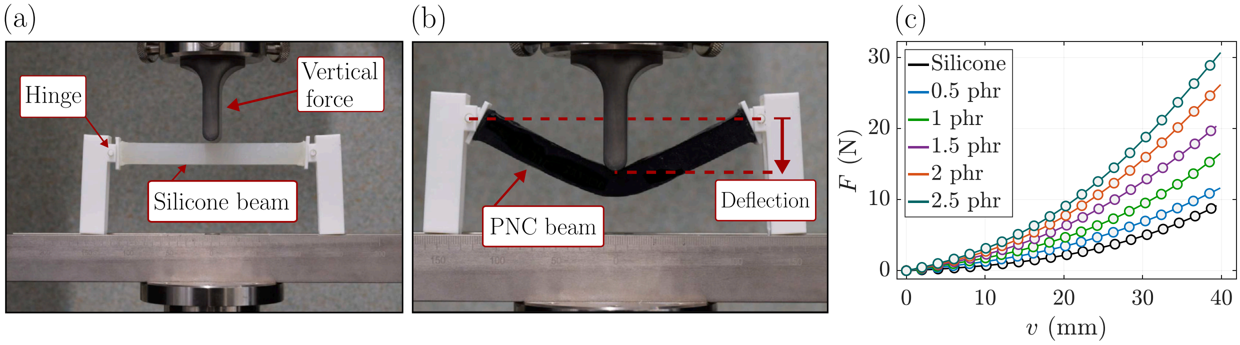

Fig. 3. Three-point bending tests on PNC beams under the hinged-hinged configuration. The beams have length 107 mm, with cross-sectional height $H = 12$ mm and width $B = 11.5$ mm. (a) Experimental setup for the silicone beam in the undeformed configuration. The beam is glued at both ends to custom-made supports which represent a hinge-type constraint. (b) PNC beam in the deformed configuration, subjected to a vertical displacement imposed at midspan. (c) Force–deflection curves obtained by increasing the imposed displacement in a quasi-static manner. Due to symmetry, the force reported in the plot corresponds to half of the experimentally measured load, consistently with the analyses presented later. Different colors, as indicated in the legend, represent beams with varying CNT contents, expressed in phr.

The internal forces are computed from Eqs. (43)–(45), where the functions f_i and g_i take the form

$$
\begin{aligned}
f_N(\lambda) &= \frac{2\left(\lambda^2-1\right)}{\lambda^{5/3}}\overline{w}_1,\\
g_N(\lambda) &= -\frac{2\left(\lambda^2+20\right)}{9\lambda^{11/3}}\overline{w}_1 + \frac{2\left(\lambda^2+5\right)}{3\lambda^{8/3}}\frac{\partial\overline{w}_1}{\partial J} + \frac{\left(\lambda^2-1\right)}{\lambda^{5/3}}\frac{\partial^2\overline{w}_1}{\partial J^2},\\
f_T(\lambda) &= \frac{2}{\lambda^{2/3}}\overline{w}_1,\\
g_T(\lambda) &= \frac{10}{9\lambda^{8/3}}\overline{w}_1 - \frac{4}{3\lambda^{5/3}}\frac{\partial\overline{w}_1}{\partial J} + \frac{1}{\lambda^{2/3}}\frac{\partial^2\overline{w}_1}{\partial J^2},\\
f_M(\lambda) &= \frac{2\left(\lambda^2+5\right)}{3\lambda^{8/3}}\overline{w}_1 + \frac{2\left(\lambda^2-1\right)}{\lambda^{5/3}}\frac{\partial\overline{w}_1}{\partial J},\\
g_M(\lambda) &= \frac{10\left(\lambda^2+44\right)}{81\lambda^{14/3}}\overline{w}_1 - \frac{2\left(\lambda^2+20\right)}{9\lambda^{11/3}}\frac{\partial\overline{w}_1}{\partial J} + \frac{\left(\lambda^2+5\right)}{3\lambda^{8/3}}\frac{\partial^2\overline{w}_1}{\partial J^2} + \frac{\left(\lambda^2-1\right)}{3\lambda^{5/3}}\frac{\partial^3\overline{w}_1}{\partial J^3}.
\end{aligned}
\tag{53}
$$

Here, $\overline{w}_1$ and its derivatives $\partial^i\overline{w}_1/\partial J^i$ are evaluated for $\kappa = 0$. For a rectangular cross-section of height H and width B, the geometric properties are

$$A = BH, \quad I_y = \frac{BH^3}{12}, \quad K_y = \frac{BH^5}{80}, \quad k_t = \frac{5}{6}. \tag{54}$$

Since the PNCs are incompressible, $\nu = 0.5$, the shear correction factor is set to

$$k_t^* = \frac{2}{3}k_t = \frac{5}{9}, \quad A_t = k_t^* A, \tag{55}$$

in order to retrieve the correct shear response.

4. Boundary value problems

In this section, we apply the proposed formulation to the finite bending of CNT-based PNC beams. First, we show the three-point bending tests performed on PNC beams with various CNT content, considering two boundary configurations: the clamped beam and the hinged beam. Then, we derive the numerical solution of the proposed beam formulation for these boundary value problems. Subsequently, we present the FE simulations performed for validation. Finally, we discuss the results.

4.1. Three-point bending tests

The specimens used in the three-point bending tests are PNC beams with initial length 107 mm, cross-sectional height $H = 12$ mm, and width $B = 11.5$ mm. Details on the specimen preparation can be found in Pelliciari et al. (2025b). Tests were first performed on beams made solely of the silicone matrix. Then, PNC beams with CNT contents of 0.5, 1, 1.5, 2 and 2.5 phr were tested. The tests for the clamped-clamped configuration are reported in Pelliciari et al. (2025b). Those for the hinged-hinged configuration are shown in Fig. 3(a)–(b). The experiments were conducted using a ZwickRoell Z050 testing machine. Both ends of the beam were glued to 3D-printed supports to reproduce hinge-type boundary conditions. Before testing, an initial longitudinal prestretch of approximately 0.05 was applied to ensure a straight initial configuration of the beam. Moreover, this prestretch caused a small

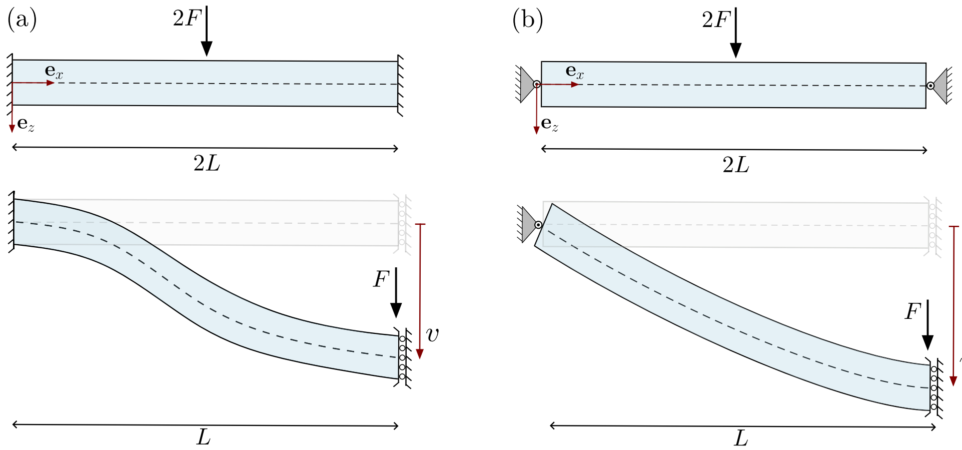

Fig. 4. Schematization of the two boundary value problems analyzed. (a) Clamped-clamped configuration and (b) hinged-hinged configuration. In both cases, the symmetry condition allowed the study of only half of the domain.

rotation of the supports, ensuring full contact with the base of the setup and preventing any movement during the test. The tests were performed under displacement control, with a wedge imposing a vertical displacement at the beam midspan at a loading rate of 20 mm/min, up to a maximum displacement of 40 mm. The resulting force–deflection curves are shown in Fig. 3(c).

4.2. Numerical solution of boundary value problems

As described in the previous section, we tested the PNC beams under two configurations: clamped and hinged. The two boundary conditions are sketched in Fig. 4. In both cases no distributed loads are applied, thus Eqs. (13) and (14) reduce to their homogeneous form. After integration and applying boundary conditions, they yield

$$N = H\cos\varphi + F\sin\varphi, \tag{56}$$

$$T = F\cos\varphi - H\sin\varphi, \tag{57}$$

where H and F are respectively the horizontal and vertical force at the boundary. In the following, dimensionless variables are introduced, as they are more convenient for numerical integration. Denoting the normalized quantities with a tilde, we define the dimensionless coordinate $\tilde{x} = x/L$, with $\tilde{x} \in [0,1]$. The normalized kinematic variables are defined as

$$\begin{aligned} &\tilde{\varphi}(\tilde{x}) = \varphi(x), \quad \tilde{\kappa}(\tilde{x}) = \kappa(x)\,L, \quad \tilde{\lambda}(\tilde{x}) = \lambda(x), \quad \tilde{\gamma}(\tilde{x}) = \gamma(x) \\ &\tilde{\mathbf{r}}_0(\tilde{x}) = \mathbf{r}_0(x)/L, \quad \tilde{\chi}(\tilde{x}) = \chi(x), \quad \tilde{\Lambda}(\tilde{x}) = \Lambda(x). \end{aligned} \tag{58}$$

We then introduce the dimensionless internal forces as

$$\widetilde{N} = N\,\frac{L^2}{E_m I_y} = \widetilde{K}_N\,\frac{f_N(\widetilde{\lambda})}{E_m} + \widetilde{\kappa}^2\,\frac{g_N(\widetilde{\lambda})}{E_m}, \tag{59}$$

$$\widetilde{T} = T\,\frac{L^2}{E_m I_y} = \widetilde{\gamma}\widetilde{K}_T\,\frac{f_T(\widetilde{\lambda})}{E_m} + \widetilde{\gamma}\widetilde{\kappa}^2\,\frac{g_T(\widetilde{\lambda})}{E_m}, \tag{60}$$

$$\widetilde{M} = M\,\frac{L}{E_m I_y} = \widetilde{\kappa}\,\frac{f_M(\widetilde{\lambda})}{E_m} + \widetilde{K}_M\widetilde{\kappa}^3\,\frac{g_M(\widetilde{\lambda})}{E_m}, \tag{61}$$

where $\widetilde{K}_N = AL^2/I_y$, $\widetilde{K}_T = A_t L^2/I_y$, $\widetilde{K}_M = K_y/(I_y L^2)$ and E_m is the elastic modulus of the matrix.

The equilibrium equations in their normalized form read

$$\widetilde{N}' = \left(-\widetilde{H}\sin\widetilde{\varphi} + \widetilde{F}\cos\widetilde{\varphi}\right)\widetilde{\kappa}, \tag{62}$$

$$\widetilde{T}' = -\left(\widetilde{F}\sin\widetilde{\varphi} + \widetilde{H}\cos\widetilde{\varphi}\right)\widetilde{\kappa}, \tag{63}$$

$$\widetilde{M}' = -\widetilde{\lambda}\,\widetilde{T} + \widetilde{\gamma}\,\widetilde{N}, \tag{64}$$

where now the prime denotes differentiation with respect to $\tilde{x}$, and $\widetilde{H} = HL^2/(E_m I_y)$, $\widetilde{F} = FL^2/(E_m I_y)$. The equilibrium equations can be reduced to a first-order system of differential equations in the kinematic variables. From Eqs. (59)–(61), the derivatives of the internal forces can be written as

$$\begin{bmatrix} \widetilde{N}' \\ \widetilde{T}' \\ \widetilde{M}' \end{bmatrix} = \begin{bmatrix} \dfrac{\partial \widetilde{N}}{\partial \widetilde{\lambda}} & 0 & \dfrac{\partial \widetilde{N}}{\partial \widetilde{\kappa}} \\ \dfrac{\partial \widetilde{T}}{\partial \widetilde{\lambda}} & \dfrac{\partial \widetilde{T}}{\partial \widetilde{\gamma}} & \dfrac{\partial \widetilde{T}}{\partial \widetilde{\kappa}} \\ \dfrac{\partial \widetilde{M}}{\partial \widetilde{\lambda}} & 0 & \dfrac{\partial \widetilde{M}}{\partial \widetilde{\kappa}} \end{bmatrix} \begin{bmatrix} \widetilde{\lambda}' \\ \widetilde{\gamma}' \\ \widetilde{\kappa}' \end{bmatrix} = \mathbf{G} \begin{bmatrix} \widetilde{\lambda}' \\ \widetilde{\gamma}' \\ \widetilde{\kappa}' \end{bmatrix} \tag{65}$$

and by inverting the Jacobian matrix $\mathbf{G}$ the first-order system of ODEs is obtained:

$$\begin{cases} \widetilde{\varphi}' = \widetilde{\kappa} \\ \widetilde{\lambda}' = \mathbf{g}^{(1)} \left[\widetilde{N}' \; \widetilde{T}' \; \widetilde{M}' \right]^T \\ \widetilde{\gamma}' = \mathbf{g}^{(2)} \left[\widetilde{N}' \; \widetilde{T}' \; \widetilde{M}' \right]^T \\ \widetilde{\kappa}' = \mathbf{g}^{(3)} \left[\widetilde{N}' \; \widetilde{T}' \; \widetilde{M}' \right]^T \\ \widetilde{r}'_{0_x} = \widetilde{\Lambda} \cos(\widetilde{\varphi} + \widetilde{\chi}) \end{cases} \tag{66}$$

where $\mathbf{g}^{(i)}$ denotes the ith row of $\mathbf{G}^{-1}$. The last equation describes the evolution of the x-component of the beam axis in the deformed configuration. System (66) represents a two-point boundary value problem which must be integrated according to boundary conditions. For the two problems considered, those are:

- clamped beam:

$$\widetilde{\varphi}(0) = 0, \quad \widetilde{\varphi}(1) = 0, \quad \widetilde{T}(0) = \widetilde{F}, \quad \widetilde{r}_{0_x}(0) = 0, \quad \widetilde{r}_{0_x}(1) = 1 + \epsilon_0, \tag{67}$$

- hinged beam:

$$\widetilde{\kappa}(0) = 0, \quad \widetilde{\varphi}(1) = 0, \quad \widetilde{T}(1) = \widetilde{F}, \quad \widetilde{r}_{0_x}(0) = 0, \quad \widetilde{r}_{0_x}(1) = 1 + \epsilon_0, \tag{68}$$

where $\epsilon_0 = 0.05$ is an initial prestretch introduced to reproduce the experimental conditions. Finally, the beam deflection is computed as

$$v = L \int_0^1 \widetilde{r}'_{0_z} d\widetilde{x} = L \int_0^1 \widetilde{\Lambda} \sin(\widetilde{\varphi} + \widetilde{\chi}) d\widetilde{x}. \tag{69}$$

System (66) was solved in MATLAB using function *bvp4c*. The solution was obtained for increasing values of the applied load F and for all CNT contents, in order to construct the force–displacement curves reported in Fig. 6. The solution at the step F_i was used as initial guess for the step F_{i+1}. The model parameters were calibrated following Appendix C.1 and are reported in Table C.1.

4.3. Finite element validation

To verify the accuracy and robustness of the beam model, FE simulations were performed using COMSOL Multiphysics. The analysis follows the approach described in Pelliciari et al. (2025b). The beam was modeled using a two-dimensional plane stress formulation. Owing to symmetry with respect to the midspan vertical axis, only half of the beam was considered. The initial half length $L = 53.5$ mm, cross-sectional height $H = 12$ mm, and cross-sectional thickness $B = 11.5$ mm were assigned according to the geometry of the tested specimens. The hyperelastic law for CNT-based polymer nanocomposites, described in Appendix B, was manually added to the software and adopted as material model. In this case, the parameters were fitted according to Appendix C.2, assuming the actual incompressible behavior of PNCs.

For both boundary configurations, a small initial prestretch was applied to replicate the experimental conditions. Coherently with the analytical model, a prestretch of $\epsilon_0 = 0.05$ was chosen and imposed through a prescribed horizontal displacement at the right end of the beam. For the clamped configuration, the vertical displacement and the rotation of the same end were constrained to zero. For the hinged configuration, the vertical displacement of the axis was fixed, whereas the cross-section was allowed to rigidly rotate around the hinge by means of a *rigid connector*. Conversely, at the left end, for both boundary configurations the vertical sliding was allowed while the horizontal displacement was fixed to zero. To remain consistent with the two-dimensional modeling, the load was distributed over a width $t = 4$ mm to account for the finite contact area with the beam surface. Finally, a stationary study was performed, incrementally increasing the applied load from an initial zero value to a final value in 50 steps. The schematization of the finite element model is shown in Fig. 5, along with the deformed configurations for both boundary conditions.

4.4. Results and discussion

Fig. 6 shows the force–deflection curves for both clamped and hinged beams at all CNT contents. The proposed model provides good predictions for all considered CNT contents over the entire range of deformation. Moreover, the model is in strong agreement

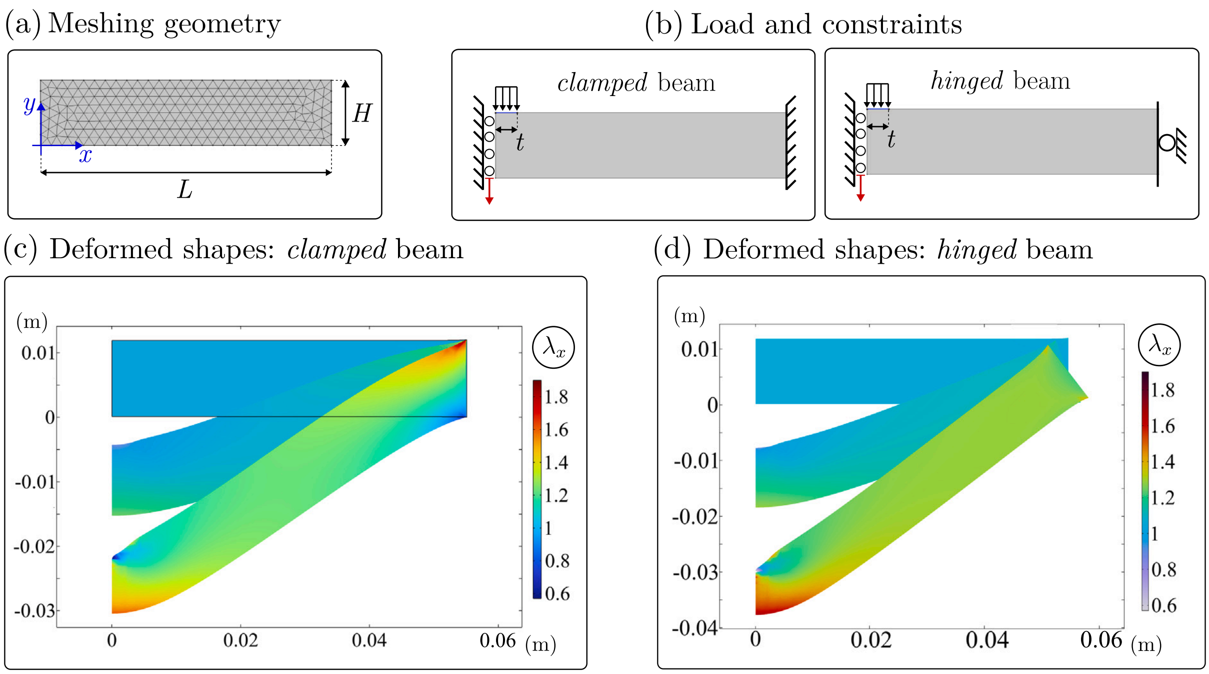

Fig. 5. COMSOL finite element simulations of PNC beams undergoing three-point bending. The material was modeled by introducing the hyperelastic law described in Appendix B as a user-defined strain energy function. The parameters were calibrated assuming the real incompressible behavior of PNCs, following Appendix C.2, and are listed in Table C.1. (a) Geometry and meshing of the 2D plane stress model. Only half of the beam was studied due to symmetry with respect to the mid-span vertical axis. (b) Boundary conditions. For both the clamped and the hinged configurations, a vertical load was applied at the left boundary over a width of t = 4 mm. (c), (d) Deformed shapes for increasing loading values and contour plot of the axial stretch λ_x for the clamped and the hinged beams, respectively.

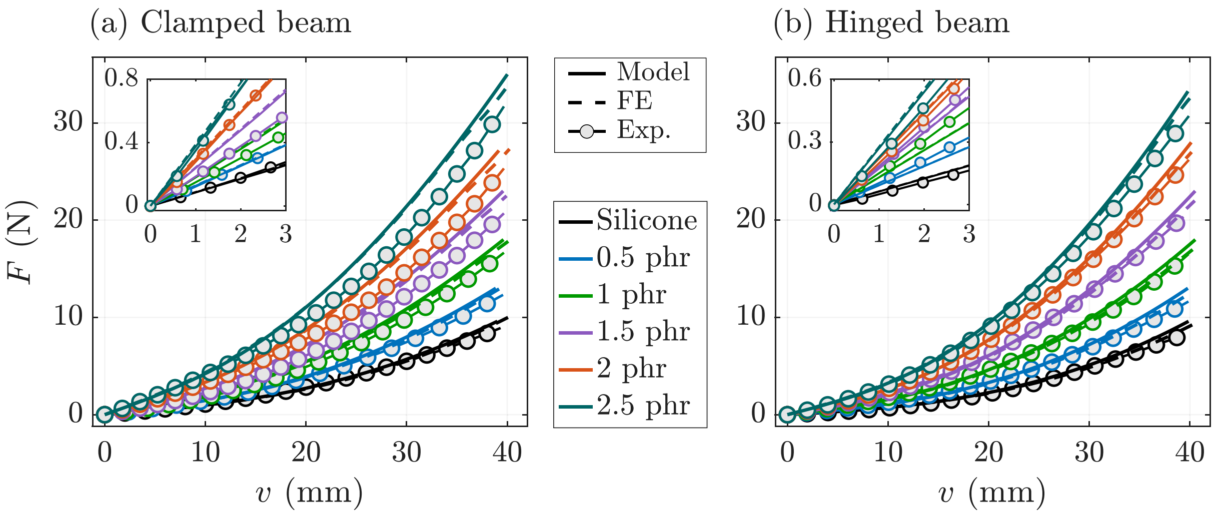

Fig. 6. Results of the model predictions (continuous lines) and comparison with experimental data (marked lines) and FE simulations (dashed lines) for different CNT contents. The results are displayed for (a) clamped beams and (b) hinged beams.

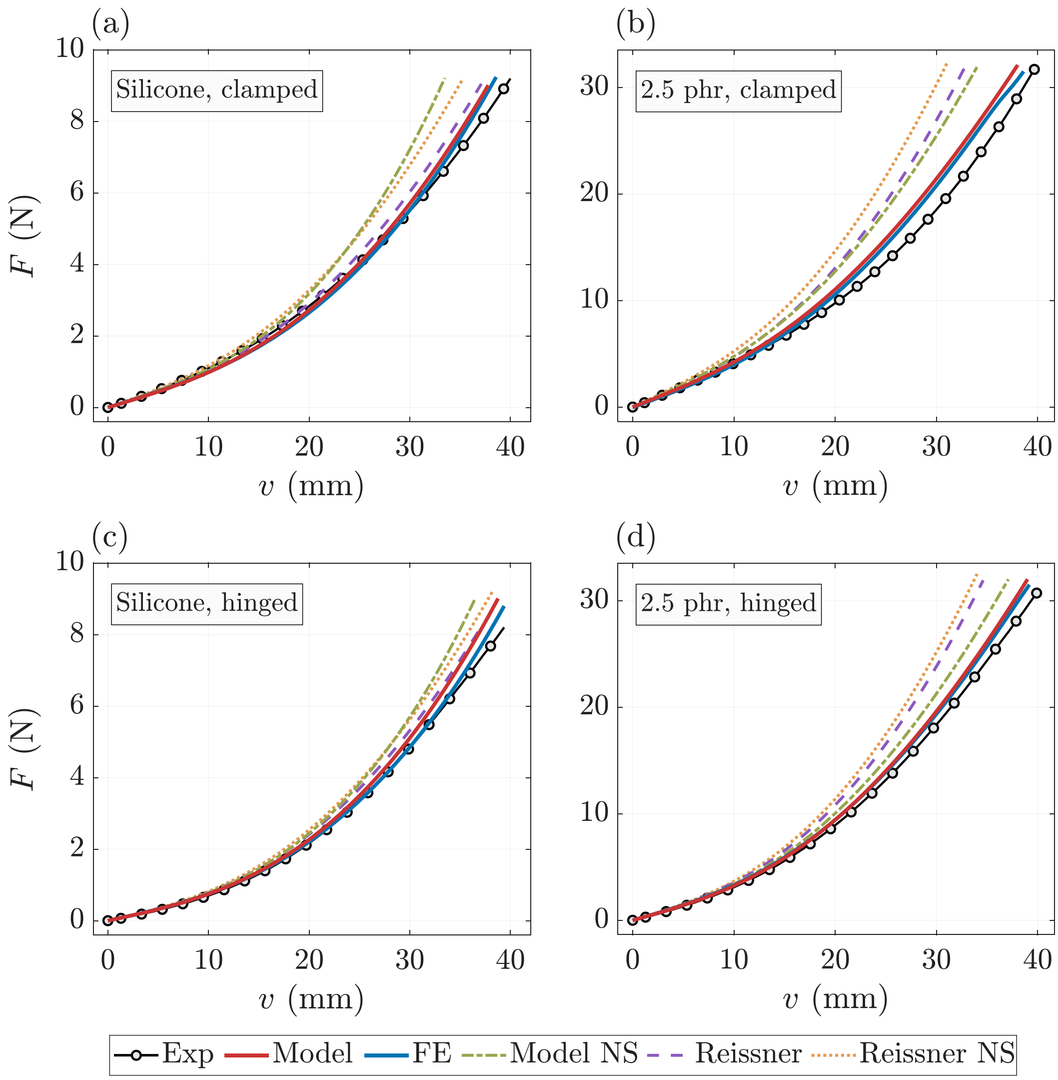

Fig. 7. Force–deflection curve predictions for different beam formulations. (a) Silicone clamped beam, (b) 2.5 phr PNC clamped beam, (c) silicone hinged beam, and (d) 2.5 phr PNC hinged beam. The following acronyms are used: Exp = experimental; Model = proposed model; FE = finite element; Model NS = proposed model without shear deformations; Reissner = Reissner model, with constitutive relations given by Eq. (70); Reissner NS = Reissner model without shear deformations, with constitutive relations given by Eq. (71). For each formulation, an initial prestretch of 0.05 was applied.

with the results provided by the FE simulations, despite the latter being obtained from a two-dimensional formulation. This consistency proves the effectiveness of the adopted continuum mechanics-based constitutive framework.

Fig. 7 compares the results obtained by the proposed model for the silicone matrix and for 2.5 phr PNC with those provided by models with simpler constitutive assumptions. The models considered are:

- the proposed model with no shear deformations (*Model NS*, green dashed lines), obtained from Eqs. (43)–(45) with $\widetilde{A}_t \to \infty$;
- the Reissner model (1972) (*Reissner*, violet dashed lines), with linear constitutive relations for the internal forces:

$$N = EA(\lambda - 1), \quad M = EI_y\kappa, \quad T = \gamma(GA_t + N); \tag{70}$$

- the Reissner model with no shear deformations (*Reissner NS*, orange dotted lines), with

$$N = EA(\lambda - 1), \quad M = EI_y\kappa, \tag{71}$$

and the shear force computed from equilibrium.

In Eqs. (70)–(71), E and G are the linear elastic and shear moduli, computed consistently for each CNT content according to Eqs. (C.6) and (C.7). As expected, all models are in agreement in the range of small-to-moderate deflections. As the deflection increases, the models considered exhibit a stiffer response than the proposed one, with increasing discrepancies. These errors are higher for PNCs with 2.5 phr CNT content, where material nonlinearities are stronger. The proposed model without shear deformations also shows discrepancies at large deflections, in particular for the clamped beams, demonstrating that shear deformation has a significant effect for the beams considered in this study. Finally, we remark again the excellent agreement between the proposed model and the FE simulations.

5. Concluding remarks

The analysis of beams undergoing large deformations has a long-standing tradition in the literature. Several authors have attempted to establish connections between beam theories and three-dimensional continuum mechanics. However, such approaches have typically been confined to specific formulations and limited classes of materials, and have not been validated against experimental data.

In this work, we presented a comprehensive formulation for the analysis of large deformations in beams made of hyperelastic materials. The kinematic description is based on the Reissner model, which accounts for axial extensibility and shear deformability of planar beams. The beam internal forces are related to the stress components of continuum mechanics through the Principle of Virtual Works. Unlike previous continuum mechanics-based studies, we clarified critical aspects involved in bridging the three-dimensional continuum and the one-dimensional beam approximation. In particular, we satisfied the beam assumption of transversely rigid cross-sections by constraining the volumetric part of the strain energy function to have a specific behavior. Closed-form expressions for the beam internal forces were derived as functions of the stress–strain response of a hyperelastic material.

We showed the implications of constraining the volumetric behavior on the choice of constitutive parameters, as a new set of parameters must be calibrated to retrieve the correct uniaxial stress–strain response of the material. As a consequence, the shear response generally differs from that of the actual material. This issue was addressed by linearizing the shear response and appropriately adjusting the shear correction factor to recover a consistent shear stiffness.

Subsequently, we specified the formulation to CNT-based PNCs, adopting the hyperelastic model proposed in our previous work. The proposed formulation was validated against experimental data from three-point bending tests on PNC beams under two distinct boundary conditions: clamped-clamped and hinged-hinged configurations. A further validation was performed through FE simulations of two-dimensional beams under plane stress conditions. The proposed formulation demonstrated good accuracy with experimental data, as well as strong agreement with the FE simulations. This can be attributed to the consistent continuum mechanics-based derivation of the constitutive relations. In addition, the proposed formulation improved upon simpler beam theories, demonstrating that both a geometrically-exact beam theory and material nonlinearities are necessary for accurate predictions of the behavior of hyperelastic beams.

The major contributions of this work can be resumed as:

- a comprehensive formulation to derive a large-displacements, large-strains one-dimensional beam theory from three-dimensional hyperelasticity;
- closed-form relations for the beam internal forces, N, T, and M, as functions of the stress–strain response of a hyperelastic material;
- application and validation of the proposed formulation against experimental data from three-point bending tests on CNT-based PNC beams. To the best of our knowledge, this represents the first application of continuum mechanics-based beam formulations to real material responses.

In conclusion, the proposed formulation combines the constitutive modeling of three-dimensional continuum mechanics within the simplicity of the one-dimensional beam theory. Therefore, it provides a foundation for the analysis of hyperelastic beams under large strains in more complex boundary value problems.

CRediT authorship contribution statement

Stefano Sirotti: Writing – review & editing, Writing – original draft, Visualization, Validation, Software, Methodology, Investigation, Formal analysis, Data curation, Conceptualization. **Matteo Pelliciari:** Writing – review & editing, Validation, Supervision, Methodology, Investigation, Funding acquisition. **Angelo Marcello Tarantino:** Supervision, Funding acquisition.

Declaration of competing interest

The authors declare that they have no known competing financial interests or personal relationships that could have appeared to influence the work reported in this paper.

Acknowledgments

The authors acknowledge the support by the Italian Ministry of University and Research (MUR) through research grants FIS 2 "PNC-Gen" (CUP E53C25000440001) and FISA-2022 "Earth-Tech" (CUP E93C24000250001). Support by the National Group of Mathematical Physics (GNFM-INdAM) is also acknowledged. The authors extend their gratitude to Eng. Manuel Pelliciari for assistance with the 3D printing of the supports for the hinge constraints used in the experiments.

Appendix A. Stress series expansion coefficients

The power-series expansion of σ_x and τ_{xz} around $\kappa = 0$ is

$$\begin{aligned}\sigma_x^* &= \sum_{n=0}^{3} \frac{1}{n!} \frac{\partial^n \sigma_x}{\partial \kappa^n}\Big|_{\kappa=0} \kappa^n + \mathcal{O}\left(\kappa^4\right), \\ \tau_{xz}^* &= \sum_{n=0}^{3} \frac{1}{n!} \frac{\partial^n \tau_{xz}}{\partial \kappa^n}\Big|_{\kappa=0} \kappa^n + \mathcal{O}\left(\kappa^4\right).\end{aligned} \tag{A.1}$$

The partial derivatives $\partial^n \sigma_x / \partial \kappa^n|_{\kappa=0}$ and $\partial^n \tau_{xz} / \partial \kappa^n|_{\kappa=0}$ are given by:

$$\begin{aligned}
\sigma_x\Big|_{\kappa=0} =& \frac{2}{\lambda^{7/3}} \left[\lambda^{2/3}\left(\lambda^2-1\right)\overline{w}_1 + \left(\lambda^2-\gamma^2-1\right)\overline{w}_2\right], \\
\frac{\partial \sigma_x}{\partial \kappa}\Big|_{\kappa=0} =& -\frac{2z}{3\lambda^{10/3}} \Bigg[\left(\lambda^2+5\right)\lambda^{2/3}\overline{w}_1 + \overline{w}_2\left(7\gamma^2-\lambda^2+7\right) + 3\frac{\partial \overline{w}_1}{\partial J}\left(\lambda^2-1\right)\lambda^{5/3} + \\
& 3\frac{\partial \overline{w}_2}{\partial J}\lambda\left(-\gamma^2+\lambda^2-1\right)\Bigg], \\
\frac{\partial^2 \sigma_x}{\partial \kappa^2}\Big|_{\kappa=0} =& -\frac{2z^2}{9\lambda^{13/3}} \Bigg[2\left(\lambda^2+20\right)\lambda^{2/3}\overline{w}_1 + \overline{w}_2\left(70\gamma^2-4\lambda^2+70\right) - 6\frac{\partial \overline{w}_1}{\partial J}\left(\lambda^2+5\right)\lambda^{5/3} - \\
& 9\frac{\partial^2 \overline{w}_1}{\partial J^2}\left(\lambda^2-1\right)\lambda^{8/3} - 6\frac{\partial \overline{w}_2}{\partial J}\lambda\left(7\gamma^2-\lambda^2+7\right) - 9\frac{\partial^2 \overline{w}_2}{\partial J^2}\lambda^2\left(-\gamma^2+\lambda^2-1\right)\Bigg], \\
\frac{\partial^3 \sigma_x}{\partial \kappa^3}\Big|_{\kappa=0} =& -\frac{2z^3}{27\lambda^{16/3}} \Bigg[10\left(\lambda^2+44\right)\lambda^{2/3}\overline{w}_1 + 14\overline{w}_2\left(65\gamma^2-2\lambda^2+65\right) + 9\lambda\Bigg(-2\frac{\partial \overline{w}_1}{\partial J}\left(\lambda^2+20\right)\lambda^{2/3} + \\
& \frac{\partial \overline{w}_2}{\partial J}\left(4\lambda^2-70\gamma^2-70\right) + 3\frac{\partial^2 \overline{w}_1}{\partial J^2}\left(\lambda^2+5\right)\lambda^{5/3} + 3\frac{\partial^3 \overline{w}_1}{\partial J^3}\left(\lambda^2-1\right)\lambda^{8/3} + \\
& 3\frac{\partial^2 \overline{w}_2}{\partial J^2}\lambda\left(7\gamma^2-\lambda^2+7\right) + 3\frac{\partial^3 \overline{w}_2}{\partial J^3}\lambda^2\left(-\gamma^2+\lambda^2-1\right)\Bigg)\Bigg], \\
\tau_{xz}\Big|_{\kappa=0} =& \frac{2\gamma}{\lambda^{4/3}}\left(\lambda^{2/3}\overline{w}_1 + \overline{w}_2\right), \\
\frac{\partial \tau_{xz}}{\partial \kappa}\Big|_{\kappa=0} =& \frac{2z\gamma}{3\lambda^{7/3}}\left[2\lambda^{2/3}\overline{w}_1 + 4\overline{w}_2 - 3\lambda\left(\frac{\partial \overline{w}_1}{\partial J}\lambda^{2/3} + \frac{\partial \overline{w}_2}{\partial J}\right)\right], \\
\frac{\partial^2 \tau_{xz}}{\partial \kappa^2}\Big|_{\kappa=0} =& \frac{2z^2\gamma}{9\lambda^{10/3}}\left[10\lambda^{2/3}\overline{w}_1 + 28\overline{w}_2 + 3\lambda\left(-4\frac{\partial \overline{w}_1}{\partial J}\lambda^{2/3} + 3\frac{\partial^2 \overline{w}_1}{\partial J^2}\lambda^{5/3} - 8\frac{\partial \overline{w}_2}{\partial J} + 3\frac{\partial^2 \overline{w}_2}{\partial J^2}\lambda\right)\right], \\
\frac{\partial^3 \tau_{xz}}{\partial \kappa^3}\Big|_{\kappa=0} =& \frac{2z^3\gamma}{27\lambda^{13/3}}\Bigg[80\lambda^{2/3}\overline{w}_1 + 280\overline{w}_2 - 9\lambda\Bigg(10\frac{\partial \overline{w}_1}{\partial J}\lambda^{2/3} + 28\frac{\partial \overline{w}_2}{\partial J} - 6\frac{\partial^2 \overline{w}_1}{\partial J^2}\lambda^{5/3} + 3\frac{\partial^3 \overline{w}_1}{\partial J^3}\lambda^{8/3} - \\
& 12\frac{\partial^2 \overline{w}_2}{\partial J^2}\lambda + 3\frac{\partial^3 \overline{w}_2}{\partial J^3}\lambda^2\Bigg)\Bigg],
\end{aligned} \tag{A.2}$$

where the partial derivatives $\overline{w}_i$, $\partial^j \overline{w}_i / \partial J^j$ are evaluated for $\kappa = 0$.

Appendix B. Strain energy function for CNT-based PNCs

The strain energy function for CNT-based polymer nanocomposites developed in our previous work (Pelliciari et al., 2025b) is

$$W_{\mathrm{PNC}}(I_1) = \left(1-\phi_f\right)W_m + \left(\phi_f - \xi\phi_a\right)W_n + \xi\phi_a W_a, \tag{B.1}$$

where W_m, W_n and W_a represent the contribution of the matrix, the nanofillers and the agglomerates respectively and have the following expressions

$$\begin{aligned}
W_m &= \frac{a}{b}\left[1 - e^{-b(I_1-3)}\right] - C_{10}\left(I_m - 3\right)\ln\left(1 - \frac{I_1-3}{I_m-3}\right), \\
W_n &= \psi_n\left(1 + \frac{\psi_n}{\Psi_n}\right)^{-1}, \quad \text{with } \psi_n = \frac{3}{8}E_n\left[\left(\frac{I_1}{3}\right)^{4/3} - 1\right], \\
W_a &= \psi_a\left(1 + \frac{\psi_a}{\Psi_a}\right)^{-1}, \quad \text{with } \psi_a = \frac{1}{2}E_a\left(\frac{I_1}{3} - 1\right).
\end{aligned} \tag{B.2}$$

The function W_m corresponds to the Yeoh-Fleming model, which proved optimal performance in capturing the nonlinear response of the tested silicone. The contributions of nanofillers and agglomerates are inspired by the concept of continuous softening hyperelasticity (Pelliciari et al., 2025a; Sirotti et al., 2025; Volokh, 2007) and involve two limiting energies, Ψ_n and Ψ_a, introducing softening with the aim of reproducing the detachment of nanofillers and agglomerates from the matrix. In Pelliciari et al. (2025b), we proposed two distinct approaches for the determination of material parameters. The first is based on microstructural considerations, with all the parameters related to the CNT contribution determined from SEM image observations; the second is a simplified, phenomenological approach, where the parameters are calibrated by fitting stress–strain data. Here we adopt the latter approach, and the following provides a complete description of the parameters involved in the formulation.

Parameter ξ represents the agglomerate volume fraction in the composite and is given by the Hill equation

$$\xi = \frac{1}{1+\left(\phi_c/\phi_f\right)^2}, \tag{B.3}$$

where ϕ_c is the critical volume fraction at which half of the nanoparticles form agglomerates and must be calibrated. Parameter ϕ_a represents the CNT fraction in the agglomerates and it is computed as

$$\phi_a = \phi_f\left(1+\rho\sqrt{e}\right), \tag{B.4}$$

where $\rho \in \left[0, \phi_c^2/(\phi_f^2\sqrt{e})\right]$ is a fitting parameter constrained to respect physical plausibility. The limiting energies Ψ_n and Ψ_a are defined as

$$\begin{aligned}\Psi_n &= \frac{3}{8}E_n\left(I_{n,cr}^{4/3}-1\right),\\ \Psi_a &= \frac{1}{2}E_a\left(I_{a,cr}-1\right),\end{aligned} \tag{B.5}$$

where $I_{n,cr}$ and $I_{a,cr}$ are critical strain invariants which identify the onset of detachment of respectively the nanofillers and the agglomerates. Finally, E_n and E_a are the *effective* elastic moduli of nanofillers and agglomerates defined according to the shear lag theory as

$$\begin{aligned}E_n &= \eta_w\eta_0\eta_n E_{\text{cnt}},\\ E_a &= \eta_w\eta_0\eta_a E_{\text{cnt}},\end{aligned} \tag{B.6}$$

where $\eta_w = 0.85$ is a waviness factor, $\eta_0 = 0.2$ is an orientation factor, $E_{\text{cnt}} = 900$ GPa is the elastic modulus of CNTs and η_n, η_a are given by

$$\begin{aligned}\eta_n &= 1-\frac{\tanh\beta_n s}{\beta_n s}, \quad \text{with } \beta_n = \sqrt{\frac{2E_m}{E_{\text{cnt}}\left(1+\nu_m\right)\ln\left(1/\phi_m\right)}},\\ \eta_a &= 1-\frac{\tanh\beta_a s}{\beta_a s}, \quad \text{with } \beta_a = \sqrt{\frac{2E_m}{E_{\text{cnt}}\left(1+\nu_m\right)\ln\left(1/\phi_a\right)}},\end{aligned} \tag{B.7}$$

where s is the aspect ratio of CNTs, E_m and ν_m are the elastic modulus and Poisson's ratio of the matrix and $\phi_m = (\phi_f - \xi\phi_a)/(1-\xi)$ is the volume fraction of CNTs outside the agglomerates.

Overall, in addition to the parameters of the matrix, the simplified model has five parameters $(\phi_c, \rho, I_{n,cr}, I_{a,cr}, s)$ to be calibrated by fitting stress–strain data.

Appendix C. Calibration of material parameters in simple tension

In this Appendix, we calibrate the material parameters of the strain energy function for PNCs by fitting simple tension data. Detailed information about the simple tension tests can be found in Pelliciari et al. (2025b). While in the tests the materials reached stretches up to $\lambda \approx 3.2$, here we focus on the range $\lambda \in [1, 2]$, which fully captures the deformations relevant to beam applications. The calibration is carried out for two scenarios: (i) considering no transverse deformation, as assumed by the proposed beam model, and (ii) considering material incompressibility, as used in the FE simulations.

C.1. Parameter calibration for the beam model

A volumetric part is added to Eq. (B.1) to allow for volume changes. Adopting the split of the energy, the complete strain energy function reads

$$W = W_{\text{PNC}}\left(\bar{I}_1\right) + W_h\left(J\right), \tag{C.1}$$

where W_{PNC} is given by Eq. (B.1), $W_h(J) = K(J-1)^2/2$ and $\bar{I}_1 = I_1/J^{2/3}$. The deformation gradient of an isotropic solid subject to simple tension in the principal direction x reads

$$\mathbf{F} = \lambda\mathbf{e}_x\otimes\mathbf{e}_x + \lambda_T\,\mathbf{e}_y\otimes\mathbf{e}_y + \lambda_T\,\mathbf{e}_z\otimes\mathbf{e}_z, \tag{C.2}$$

where the transverse stretch is equal in both directions due to isotropy. To satisfy the beam model assumption of transversely rigid cross-sections, we impose $\lambda_T = 1$ to neglect transverse deformations. The nominal stress is computed as

$$\mathbf{P} = \frac{\partial W}{\partial \mathbf{F}} = P_{xx}\mathbf{e}_x\otimes\mathbf{e}_x + P_{yy}\mathbf{e}_y\otimes\mathbf{e}_y + P_{yy}\mathbf{e}_z\otimes\mathbf{e}_z. \tag{C.3}$$

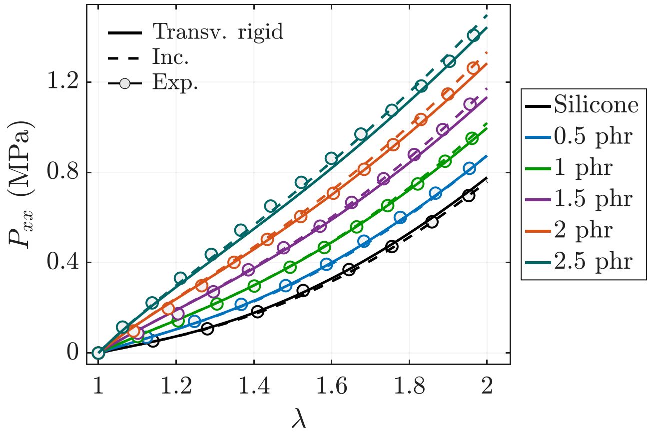

Fig. C.8. Parameter calibration by fitting to nominal stress–strain data from simple tension tests. Solid lines denote the response of the transversely rigid material, Eq. (C.4), adopted for the beam model. Dashed lines represent the response of the incompressible material adopted in FE simulations, Eq. (C.10).

Table C.1
Optimal parameters for the beam model and the FE simulations, calibrated against stress–strain data from simple tension tests. When applicable, the units are in MPa.

Parameters	Matrix				CNT					Fixed		
	a	b	C_{10}	I_m	ϕ_c	ρ	$I_{n,\mathrm{cr}}$	$I_{a,\mathrm{cr}}$	s	E_{cnt}	η_w	η_0
Beam model	−7.508 ($E_m = 0.378,\ \nu_m = 0$)	0.051	7.602	279	0.05	0.8	300	200	120	9×10^5	0.85	0.2
FE model	−0.511 ($E_m = 0.378,\ \nu_m = 0.5$)	0.163	0.574	102	0.03	0.8	30	20	119			

Imposing that the lateral surfaces of the solid are traction-free, $P_{yy} = 0$, the expression for K is determined. Finally, the only non-vanishing stress component, $P_{xx} = (1-\phi_f)P_{m_{xx}} + P_{\mathrm{CNT}_{xx}}$, becomes

$$P_{m_{xx}} = \frac{2\left(\lambda^2-1\right)}{\lambda^{5/3}}\left[a e^{-b(\bar{I}_1-3)} + C_{10}\frac{I_m-3}{I_m-\bar{I}_1}\right],$$
$$P_{\mathrm{CNT}_{xx}} = \frac{2\left(\lambda^2-1\right)}{\lambda^{5/3}}\left[\frac{6E_a\xi\Psi_a^2\phi_a}{\left(E_a\bar{I}_1-3E_a+6\Psi_a\right)^2} + \frac{32\ E_n\left(9\bar{I}_1\right)^{1/3}\Psi_n^2\left(\phi_f-\xi\phi_a\right)}{\left(3^{2/3}E_n\bar{I}_1^{4/3}-9E_n+24\Psi_n\right)^2}\right], \tag{C.4}$$

with $\bar{I}_1 = (\lambda^2+2)/\lambda^{2/3}$. The matrix parameters a, b, C_{10}, and I_m were first calibrated by fitting the response of the silicone matrix. Subsequently, the parameters of CNT contribution, ϕ_c, ρ, $I_{n,cr}$, $I_{a,cr}$, and s were calibrated following the strategy illustrated in Pelliciari et al. (2025b). The result of the fitting is shown in Fig. C.8 (solid lines) and the optimal parameters are reported in Table C.1.

The linearization of P_{xx} about $\lambda = 1$ yields

$$P_{xx} = \left[4\left(a+C_{10}\right)\left(1-\phi_f\right) + \frac{2}{3}\xi\phi_a\left(E_a-E_n\right) + \frac{2}{3}E_n\phi_f\right](\lambda-1) + \mathcal{O}\left((\lambda-1)^2\right), \tag{C.5}$$

where

$$E_{\mathrm{rig}} = 4\left(a+C_{10}\right)\left(1-\phi_f\right) + \frac{2}{3}\xi\phi_a\left(E_a-E_n\right) + \frac{2}{3}E_n\phi_f \tag{C.6}$$

is the elastic modulus of the transversely rigid material. The corresponding shear modulus is

$$G_{\mathrm{rig}} = \frac{E_{\mathrm{rig}}}{2} = 2(a+C_{10})(1-\phi_f) + \frac{1}{3}\xi\phi_a(E_a-E_n) + \frac{1}{3}E_n\phi_f. \tag{C.7}$$

C.2. Parameter calibration for FE simulations

In the FE simulations we assume the actual volumetric behavior of PNCs, which are considered to be incompressible. The strain energy function is thus given by Eq. (B.1). The deformation gradient reads

$$\mathbf{F} = \lambda\mathbf{e}_x\otimes\mathbf{e}_x + \lambda^{-1/2}\ \mathbf{e}_y\otimes\mathbf{e}_y + \lambda^{-1/2}\ \mathbf{e}_z\otimes\mathbf{e}_z, \tag{C.8}$$

where the lateral stretch is now determined by the incompressibility constraint $\lambda\lambda_T^2 = 1$. The nominal stress is computed as

$$\mathbf{P} = \frac{\partial W}{\partial \mathbf{F}} - p\mathbf{F}^{-T} = P_{xx}\mathbf{e}_x \otimes \mathbf{e}_x + P_{yy}\mathbf{e}_y \otimes \mathbf{e}_y + P_{yy}\mathbf{e}_z \otimes \mathbf{e}_z, \tag{C.9}$$

where the internal pressure p is determined by satisfying the condition $P_{yy} = 0$. The expression of the longitudinal stress $P_{xx} = (1-\phi_f)P_{m_{xx}} + P_{\mathrm{CNT}_{xx}}$ becomes

$$\begin{aligned} P_{m_{xx}} &= 2\left(\lambda - \frac{1}{\lambda^2}\right)\left[ae^{-b(I_1-3)} + C_{10}\frac{I_m - 3}{I_m - I_1}\right], \\ P_{\mathrm{CNT}_{xx}} &= 2\left(\lambda - \frac{1}{\lambda^2}\right)\left[\frac{6E_a\xi\Psi_a^2\phi_a}{\left(E_aI_1 - 3E_a + 6\Psi_a\right)^2} + \frac{32\ 3^{2/3}E_nI_1^{1/3}\Psi_n^2\left(\phi_f - \xi\phi_a\right)}{\left(3^{2/3}E_nI_1^{4/3} - 9E_n + 24\Psi_n\right)^2}\right], \end{aligned} \tag{C.10}$$

with $I_1 = \lambda^2 + 2/\lambda$. For the matrix parameters, we adopted the set already calibrated in Pelliciari et al. (2025b) on the silicone matrix response. The CNTs parameters were calibrated following the same procedure as in the previous section and are reported in Table C.1. The result of the fitting is shown in Fig. C.8 (dashed lines). We verified to obtain similar values for the elastic modulus in order to ensure a consistent comparison between the beam model and the FE simulations. For the incompressible material, the linearization of P_{xx} about $\lambda - 1$ yields

$$P_{xx} = \left[6\left(a + C_{10}\right)\left(1-\phi_f\right) + \xi\phi_a\left(E_a - E_n\right) + E_n\phi_f\right](\lambda - 1) + \mathcal{O}\left((\lambda-1)^2\right), \tag{C.11}$$

where

$$E_{\mathrm{inc}} = 6\left(a + C_{10}\right)\left(1-\phi_f\right) + \xi\phi_a\left(E_a - E_n\right) + E_n\phi_f \tag{C.12}$$

is the linear elastic modulus. The corresponding shear modulus is

$$G_{\mathrm{inc}} = \frac{E_{\mathrm{inc}}}{3} = 2\left(a + C_{10}\right)\left(1-\phi_f\right) + \frac{1}{3}\xi\phi_a\left(E_a - E_n\right) + \frac{1}{3}E_n\phi_f. \tag{C.13}$$

This expression coincides with the shear modulus for the transversely rigid material, Eq. (C.7), as the difference between the two cases lies solely in the volumetric response. However, since the two sets of parameters were calibrated to ensure $E_{\mathrm{rig}} = E_{\mathrm{inc}}$, it follows that

$$G_{\mathrm{rig}} = \frac{E_{\mathrm{rig}}}{2} = \frac{E_{\mathrm{inc}}}{2} = \frac{3}{2}G_{\mathrm{inc}}, \tag{C.14}$$

indicating that the shear modulus of the transversely rigid material results 1.5 times larger than that of the incompressible material. Consequently, in Eq. (55) the shear correction factor k_t was adjusted accordingly to recover the correct response in simple shear.

Data availability

Data will be made available on request.

References

Attard, M. M. (2003). Finite strain–beam theory. *International Journal of Solids and Structures*, *40*(17), 4563–4584.

Attard, M. M., & Hunt, G. W. (2008). Sandwich column buckling–A hyperelastic formulation. *International Journal of Solids and Structures*, *45*(21), 5540–5555.

Attard, M. M., & Kim, M.-Y. (2010). Lateral buckling of beams with shear deformations–A hyperelastic formulation. *International Journal of Solids and Structures*, *47*(20), 2825–2840.

Batista, M. (2016). A closed-form solution for Reissner planar finite-strain beam using Jacobi elliptic functions. *International Journal of Solids and Structures*, *87*, 153–166.

Boyce, M. C., & Arruda, E. M. (2000). Constitutive models of rubber elasticity: a review. *Rubber Chemistry and Technology*, *73*(3), 504–523.

Cantournet, S., Boyce, M. C., & Tsou, A. H. (2007). Micromechanics and macromechanics of carbon nanotube-enhanced elastomers. *Journal of the Mechanics and Physics of Solids*, *55*(6), 1321–1339.

Engesser, F. (1891). *Die knickfestigkeit gerader stäbe*. W. Ernst & Sohn.

Euler, L. (1744). *Methodus inveniendi lineas curvas... sive solutio problematis isoperimetrici.(cum tabulis aeneis)*. Marcus-Michael Bousquet.

Falope, F. O., Lanzoni, L., & Tarantino, A. M. (2019). The bending of fully nonlinear beams. Theoretical, numerical and experimental analyses. *International Journal of Engineering Science*, *145*, Article 103167.

Firouzi, N., Lenci, S., Amabili, M., & Rabczuk, T. (2024). Nonlinear free vibrations of Timoshenko–Ehrenfest beams using finite element analysis and direct scheme. *Nonlinear Dynamics*, *112*(9), 7199–7213.

Fu, S., Sun, Z., Huang, P., Li, Y., & Hu, N. (2019). Some basic aspects of polymer nanocomposites: A critical review. *Nano Materials Science*, *1*(1), 2–30.

Haringx, J. (1942). On the buckling and lateral rigidity of helical springs. *Proceedings of the Koninklijke Nederlandse Akademie Van Wetenschappen / Biological, Chemical, Geological, Physical and Medical Sciences*, *45*(533), 142.

Humer, A. (2013). Exact solutions for the buckling and postbuckling of shear-deformable beams. *Acta Mechanica*, *224*(7), 1493–1525.

Humer, A., & Irschik, H. (2009). Large deflections of beams with an unknown length of the reference configuration. In *50th AIAA/ASME/ASCE/AHS/ASC structures, structural dynamics, and materials conference 17th AIAA/ASME/AHS adaptive structures conference 11th AIAA no* (p. 2371).

Humer, A., & Irschik, H. (2011). Large deformation and stability of an extensible elastica with an unknown length. *International Journal of Solids and Structures*, *48*(9), 1301–1310.

Irschik, H., & Gerstmayr, J. (2009). A continuum mechanics based derivation of Reissner's large-displacement finite-strain beam theory: the case of plane deformations of originally straight Bernoulli–Euler beams. *Acta Mechanica*, *206*(1), 1–21.
Irschik, H., & Gerstmayr, J. (2011). A continuum-mechanics interpretation of Reissner's non-linear shear-deformable beam theory. *Mathematical and Computer Modelling of Dynamical Systems*, *17*(1), 19–29.
Islam, S., Yang, S., & Kim, C. I. (2023). A multiscale continuum model for the mechanics of hyperelastic composite reinforced with nanofibers. *International Journal of Solids and Structures*, *267*, Article 112168.
Kim, H., Abdala, A. A., & Macosko, C. W. (2010). Graphene/polymer nanocomposites. *Macromolecules*, *43*(16), 6515–6530.
Lenci, S., & Rega, G. (2016). Nonlinear free vibrations of planar elastic beams: a unified treatment of geometrical and mechanical effects. *Procedia IUTAM*, *19*, 35–42.
Lubbers, L. A., van Hecke, M., & Coulais, C. (2017). A nonlinear beam model to describe the postbuckling of wide neo-Hookean beams. *Journal of the Mechanics and Physics of Solids*, *106*, 191–206.
Magnusson, A., Ristinmaa, M., & Ljung, C. (2001). Behaviour of the extensible elastica solution. *International Journal of Solids and Structures*, *38*(46–47), 8441–8457.
Maqueda, L. G., & Shabana, A. A. (2007). Poisson modes and general nonlinear constitutive models in the large displacement analysis of beams. *Multibody System Dynamics*, *18*(3), 375–396.
Matos, M. A., Tagarielli, V. L., Baiz-Villafranca, P. M., & Pinho, S. T. (2018). Predictions of the electro-mechanical response of conductive CNT-polymer composites. *Journal of the Mechanics and Physics of Solids*, *114*, 84–96.
Miculescu, M., Thakur, V. K., Miculescu, F., & Voicu, S. I. (2016). Graphene-based polymer nanocomposite membranes: a review. *Polymers for Advanced Technologies*, *27*(7), 844–859.
Moniruzzaman, M., & Winey, K. I. (2006). Polymer nanocomposites containing carbon nanotubes. *Macromolecules*, *39*(16), 5194–5205.
Palmov, V. A. (1998). *Vibrations of elasto-plastic bodies*. Springer Science & Business Media.
Paradiso, M., Dal Corso, F., & Bigoni, D. (2025). A nonlinear model of shearable elastic rod from an origami-like microstructure displaying folding and faulting. *Journal of the Mechanics and Physics of Solids*, *200*, Article 106100.
Pelliciari, M., Sirotti, S., Aloisio, A., & Tarantino, A. M. (2025a). Hyperelastic model for nonlinear elastic deformations of graphene-based polymer nanocomposites. *International Journal of Solids and Structures*, *308*, Article 113144.
Pelliciari, M., Sirotti, S., & Tarantino, A. M. (2025b). A microstructure-informed hyperelastic model for CNT-based polymer nanocomposites under large deformations. *International Journal of Solids and Structures*, Article 113779.
Qin, Y., Peng, Q., Ding, Y., Lin, Z., Wang, C., Li, Y., Xu, F., Li, J., Yuan, Y., He, X., & Li, Y. (2015). Lightweight, superelastic, and mechanically flexible graphene/polyimide nanocomposite foam for strain sensor application. *ACS Nano*, *9*(9), 8933–8941.
Reissner, E. (1972). On one-dimensional finite-strain beam theory: the plane problem. *Zeitschrift Für Angewandte Mathematik Und Physik ZAMP*, *23*(5), 795–804.
Rivlin, R. S. (1948). Large elastic deformations of isotropic materials IV. Further developments of the general theory. *Philosophical Transactions of the Royal Society of London. Series A, Mathematical and Physical Sciences*, *241*(835), 379–397.
Sadd, M. H. (2018). *Continuum mechanics modeling of material behavior*. Academic Press.
Sansour, C. (2008). On the physical assumptions underlying the volumetric-isochoric split and the case of anisotropy. *European Journal of Mechanics. A. Solids*, *27*(1), 28–39.
Simo, J. C. (1988). A framework for finite strain elastoplasticity based on maximum plastic dissipation and the multiplicative decomposition: Part I. Continuum formulation. *Computer Methods in Applied Mechanics and Engineering*, *66*(2), 199–219.
Simo, J. C., Hjelmstad, K. D., & Taylor, R. L. (1984). Numerical formulations of elasto-viscoplastic response of beams accounting for the effect of shear. *Computer Methods in Applied Mechanics and Engineering*, *42*(3), 301–330.
Sirotti, S., Pelliciari, M., Aloisio, A., & Tarantino, A. M. (2025). A strain energy function for the inflation of hyperelastic membranes. *Mechanics of Materials*, *209*, Article 105442.
Treloar, L. G. (1975). The physics of rubber elasticity.
Volokh, K. Y. (2007). Hyperelasticity with softening for modeling materials failure. *Journal of the Mechanics and Physics of Solids*, *55*(10), 2237–2264.
Wang, Q., & Zhu, L. (2011). Polymer nanocomposites for electrical energy storage. *Journal of Polymer Science Part B: Polymer Physics*, *49*(20), 1421–1429.
Ziegler, H. (1982). Arguments for and against Engesser's buckling formulas. *Ingenieur-Archiv*, *52*(1), 105–113.